Journal of Simulation & Analysis of Novel Technologies in Mechanical Engineering
10 (2) (2017) 0005~0012
HTTP://JSME.IAUKHSH.AC.IR
ISSN: 2008-4927

Investigation of Shape Functions Role on the Mesh-free Method Application in Soft Tissue Elastography

Hamed Ajabi Naeeni[1,*], Mohammad Haghpanahi[2], Hamid Behnam[3], Hadi Pirali[2]

1- Department of Mechanical Engineering, Khomeinishahr Branch, Islamic Azad University, Isfahan, 84175-119, Iran.

2- Department of Mechanical Engineering, Iran University of Science and Technology, Tehran, Iran

3- Department of Electrical Engineering, Iran University of Science and Technology, Tehran, Iran

**Corresponding Author: Ajabinaeeni@iaukhsh.ac.ir*

(Manuscript Received --- 09, 2016; Revised --- 12, 2016; Accepted --- 02, 2017; Online --- 07, 2017)

Abstract

In current study, The Mesh-free method based on weak-form formulation coupled with the ultrasound imaging technique is developed. This problem consists in computing the deformation of an elastic non-homogenous phantom by numerical methods (both Mesh-free and Finite Element) and converge their results to the measured deformation by the ultrasound. The shape functions of Mesh-free are approximated by the Moving Least Square (MLS) method. The effect of Shape functions on the Mesh-free results are analyzed and discussed with the several simulations in 2D domain.

Keywords: Elastography, Mesh-free, Soft Tissue Phantom.

1- Introduction

Elastography is an imaging technique that presents insight into the mechanical properties of soft tissues by applying a mechanical stimulation and then imaging the resulting local displacements[1-5].

It is difficult to explain the correct mechanical behavior of biological tissue under loading exactly, and one can assume that accurate determinations of the mechanical characteristics of a tissue from its behavior under load through use of a mathematical model are actually difficult to attain and disposed to error.

Elastography techniques make use of some types of models to generate and estimate of quantitative elasticity; hence, they all experience errors that arise from the inevitable shortcomings in their respective model descriptions. However, images taken in elastography modalities occur in different geometries, so making comparison difficult. In order to confirm significant correlation of imaging data, a mean of mapping or co-registering one image into another in a physically accurate method is needed [6].

Nowadays, computational biomechanics has appeared as a topic of considerable interest to the medical image analysis community. Some of the particular utilities are methods for modeling soft tissue deformation. The most physically consistent models are those based on equations of continuum mechanics, which

are generally solved using a numerical technique such as the finite element (FE) method[7].

The concept of the finite element method is to division of the tissue volume into the network of elements called mesh, to set up governing equations for each element, and then to assemble all element equilibrium equations into a system of equations.

This method is recognized for the modeling of complex problems in biomechanics. It is a developed method, but it is not without shortcomings. The dependency of this technique on a mesh conducts to difficulties for several classes of problem. Significant loss in accuracy occurs in problems of crack propagation, large deformations, shell problems, phase transformation, movement of free surface and strain localization. The application of a mesh in modeling of these problems makes problems in the handling of discontinuities, which do not coincide to initial mesh lines. This is due to the basic properties of an element-based shape function. Also, in the finite element method, mesh generation is a far more time-consuming and costly task than the assembly and solution of the finite element equations.

One of powerful numerical method is mesh-free method that does not need any element for shape function construction. Meshfree methods have performed as connectivity free between elements and nodes.

Present research is studied the applicability of mesh-free method to predict soft tissue deformation was validated with ultrasound imaging of heterogeneous tissue mimicking phantom and FEM.

The paper is organized as follows: Firstly, the materials and methods consist of theory of Meshfree method and the data acquisition of both experiment and numerical simulation are presented. Secondly, meshfree modeling of phantom is conducted and a comparison of the calculated motion and the measured motion is completed. Finally, using the mesh-free method in predicting of soft tissue deformation is validated and the conclusion is drawn.

2- Materials and Methods

2-1- Theory

The most generally used estimation theories in mesh-free methods are the moving-least squares (MLS) approximation in the element-free Galerkin (EFG) method. The discretization of the governing equations by element-free Galerkin method needs moving least square interpolation functions which are constituted of three main part[8]:

1) a weight function,

2) a monomial basis function and

3) a set of coefficients.

If an unknown scalar function of a field variable $u(\mathrm{x})$ is approximated by $u^h(\mathrm{x})$ over the two-dimensional domain Ω, The MLS approximation of $u(\mathrm{x})$ is defined as:

$$u^h(\mathbf{x}) = \sum_{j=1}^{m} p_j(\mathbf{x}) a_j(\mathbf{x}) = \mathrm{p}^T(\mathbf{x})\mathrm{a}(\mathbf{x}) \qquad (1)$$

Where $a_j(\mathbf{x})$ is the non-constant coefficients, $\mathrm{x}^{\mathrm{T}}=[x,y]$ for two dimensional problem, and $p_j(\mathbf{x})$ is basis function often built using monomials from the Khayyam-Pascal triangle to confirm minimum completeness as below:

$$\begin{array}{ll} \mathbf{p}^{\mathrm{T}} = \begin{bmatrix} 1 & \mathrm{x} & \mathrm{y} \end{bmatrix} & \mathrm{m}=3 \\ \mathbf{p}^{\mathrm{T}} = \begin{bmatrix} 1 & \mathrm{x} & \mathrm{y} & \mathrm{x}^2 & \mathrm{xy} & \mathrm{y}^2 \end{bmatrix} & \mathrm{m}=6 \end{array} \qquad (2)$$

Which m is the number of the basic functions.

The coefficients $a_j(\mathbf{x})$ are obtained by minimizing the quadratic functional $\mathbf{J}(x)$ as follow.

$$\begin{aligned}\mathbf{J}(\mathbf{x}) &= \sum_{i=1}^{n} w(x-x_i)[u^h(x) - u_i]^2 \\ &= \sum_{i=1}^{n} w(x-x_i)[\mathbf{p}^T(x_i)\mathbf{a}(x) - u_i]^2\end{aligned} \tag{3}$$

Where n is the number of nodes in the support domain of x, $w(\mathbf{x}-\mathbf{x}_i)$ is a weight function with domain of influence and u_i is the nodal parameter of u at x_i.

To find the coefficients a(x), it should be calculated the minimum of J which leads to the following set of linear relations:

$$\mathbf{a}(x) = \mathbf{A}^{-1}(x)\mathbf{B}(x)\,\mathbf{U}_s \tag{4}$$

Where A and B are defined by:

$$\mathbf{A} = \mathbf{p}^T\mathbf{w}(x)\,\mathbf{p} \tag{5}$$

$$\mathbf{B} = \mathbf{p}^T\mathbf{w}(x) \tag{6}$$

Substituting the above equation back into MLS approximation of $u(x)$ (Eq. 1), it obtains:

$$u^h(\mathbf{x}) = \sum_{i=1}^{n} \Phi_i(x)u_i = \mathbf{\Phi}^T(x)\mathbf{U}_s \tag{7}$$

Where the vector of MLS shape functions corresponding n nodes in the support domain of the point x, $\mathbf{\Phi(x)}$, is defined by:

$$\mathbf{\Phi}^T(\mathbf{x}) = \sum_{i=1}^{n}\Phi_i = \sum_{i=1}^{n}\sum_{j=0}^{m} p_j(x)(\mathbf{A}^{-1}(x)\mathbf{B}(x))_{ji} \tag{8}$$

Figure 1 is illustrated the MLS shape functions created using 25 nodes with regular dispersion in the support domain and different type of basis function (m=3 and m=6).

The weight function is non-zero at the small region of around the node, called support domain of the node. The cubic spline function used in this study has two order of continuity and can be written as a function of normalized radius $\bar{r}$ as below:

$$w_i(x) = \begin{cases} \frac{2}{3} - 4\bar{r}^2 + 4\bar{r}^3 & \bar{r} \le 0.5 \\ \frac{4}{3} - 4\bar{r} + 4\bar{r}^2 - \frac{4}{3}\bar{r}^3 & 0.5 \le \bar{r} \le 1 \\ 0 & \bar{r} > 1 \end{cases} \tag{9}$$

Where

$$\bar{r}_i = \frac{|\mathbf{x} - \mathbf{x}_i|}{d_s} \tag{10}$$

in which $|\mathbf{x} - \mathbf{x}_i|$ is the distance from node x_i to the sampling point x, and $d_s = \alpha_s . d_c$ is the size of the support domain for the weight function that is computed by multiplying the scaling parameter , α_s ,into nodal spacing, d_c .

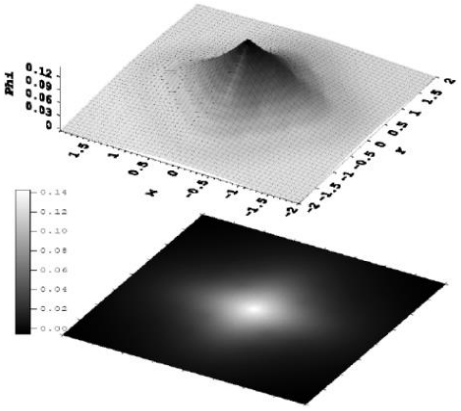

(a) linear basis function (m=3)

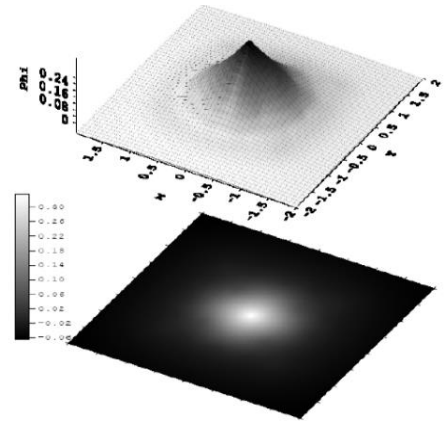

(b) Quadratic basis function (m=6)

Fig. 1- MLS shape function for center node

3- Numerical Simulation

FE simulation is performed using the ABAQUS 6.6.1 to investigate the performance of mesh-free method in simulation of heterogeneous media. A rectangular 100mm × 100mm phantom containing one circular hard inclusion with 10mm of radius is simulated under the plane-strain state with respect to experiment (Fig. 2). The Poisson's ratio of the inclusion and the surrounding media is set to be 0.495(near incompressible).

In order to reconstruct the elastic modulus, the boundary data related to experiment is applied to the model as follows: on the top of boundary three amount linear distributed loads are applied. All nodes on the bottom and left and right sides boundary are fixed. The phantom is 2-D and is made up of 2400 4-noded plane strain elements.

The ideal displacement field can be obtained by solving this problem. By comparing the calculated displacement in one direction with measured displacement in the experiment at the same direction, and converging the numerical result to the experiment, the elastic modulus of phantom can be estimated[9].

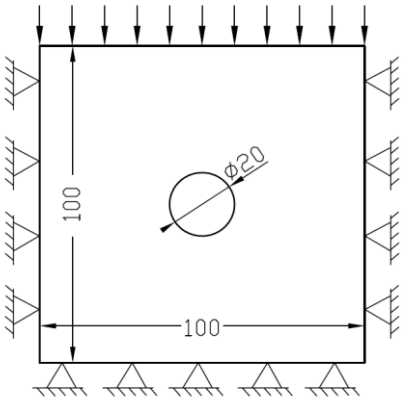

Fig. 2- Schematic of Problem

4- Validation

To determine the reliability of experiment and to validate the numerical results, the uniaxial compression test is applied on four cylindrical samples of each part of phantom (soft background and hard inclusion) using Zwick 1446 mechanical testing system. Fig. 3 shows the setup of uniaxial compression test[10].

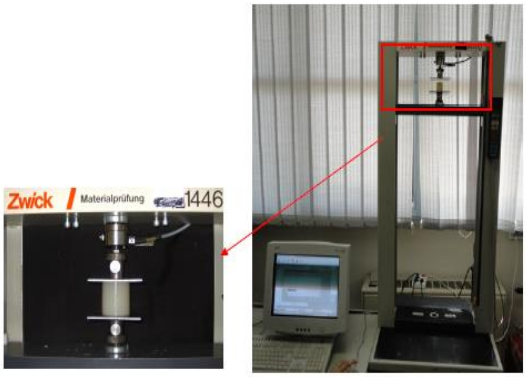

Fig. 3- Uniaxial compression test to determine the elastic modulus of each part of phantom.

5- Results

The displacement distribution obtained by FEM and Meshfree method are displayed in Fig. 4, including the displacement field, u_y in third loading. The elasticity of the above models are obtained after convergency of numerical modeling results and experiment results. The elasticity of the surrounding phantom material and embedded inclusion are 500kPa and 800kPa, respectively. The vertical displacement along dotted line in Fig. 4 is plotted in Fig. 5.

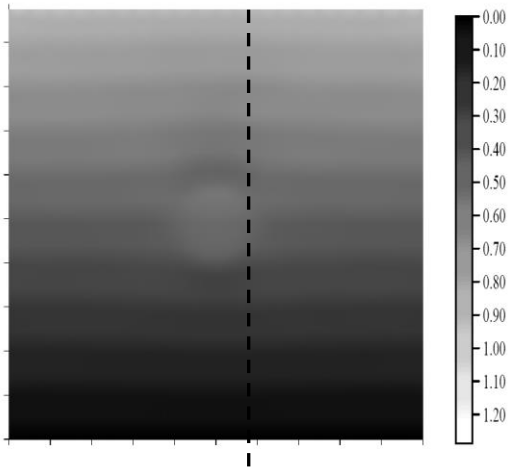

(a)

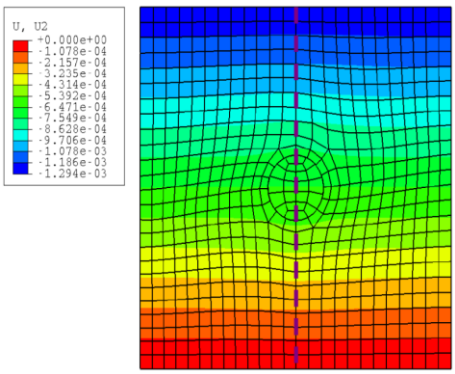

(b)

Fig. 4- 2D vertical displacement field obtained by a)Meshfree; b)FE

Young's modulus of two parts of the phantom materials measured by uniaxial compression test is shown in table 1.

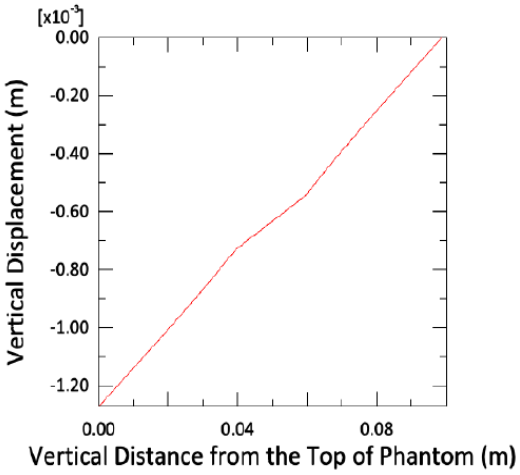

Fig. 5- Vertical displacement from top to end of the phantom along dotted line in Fig. 4. The fracture at the point A shows the location of harder inclusion.

Table 1- Young's modulus of the phantom materials calculated by uniaxial compression test

Sample Type	Elasticity Modulus (kPa) Using Uniaxial Compression Test	Elasticity Modulus (kPa) Using Modeling	Error (%)
Harder Inclusion	795±25	800	0.6
Surrounding Media	485±20	500	3

6- Discussion and Conclusion

The fracture at the point A shows the location of harder inclusion. Three amount of loading are performed on the heterogeneous tissue mimicking phantom and related displacement field of the phantom is calculated using 2 types of numerical method, Finite Element and Meshfree method. The real displacement of the phantom is measured by speckle tracking of ultrasound images pixel named optical flow. By changing the elastic modulus of two types of phantom material and converging the numerical displacement results to the real displacement measured by optical flow technique, the elastic modulus can be estimated as 800kPa and 500kPa, respectively for hard inclusion and soft background. These amounts of elastic modulus are in good agreement with uniaxial compression test results which are performed on related types of phantom material and mentioned in table 1.

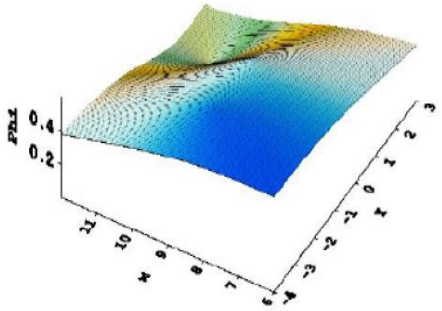

a- $\alpha_s = 1$*; 3 nodes in the support domain*

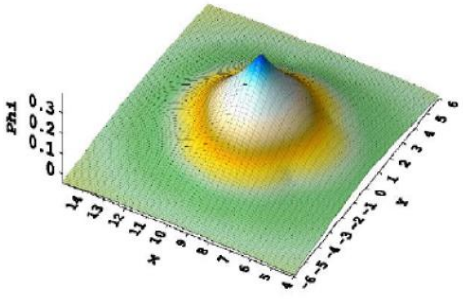

b- $\alpha_s = 2$*; 13 nodes in the support domain*

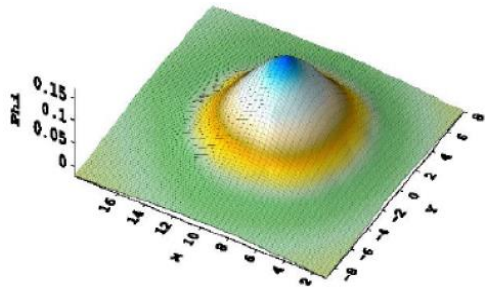

c- $\alpha_s = 3$ *; 27 nodes in the support domain*

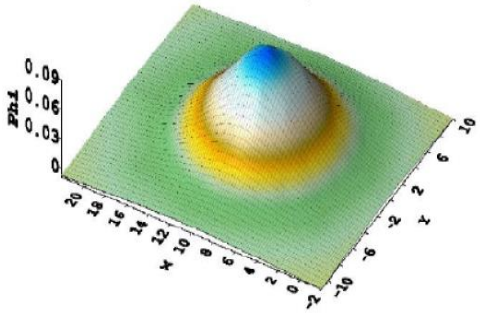

d- $\alpha_s = 4$ *; 52 nodes in the support domain*

Fig. 6- Effect of support domain size on the shape function of node A which specified in Fig. 5

The MLS shape functions, Phi, for the central node (x=0, y=0) using different type of basis function are plotted in Fig. 1. One can see, when the order of basis function, m, becomes larger, the shape function, phi, increases and the performance of the MLS approximation will be improved because of possessing the Kronecker delta condition. But, if the number node in support domain is smaller than the number of basis function, the moment matrix A in equation (4), isn't invertible.

In Fig. 6, the effect of support domain size on the shape function is shown. One can see when the size of support domain increase, the shape function is further to Kronecker delta property. In the other hand, when the size of support domain is too small, the shape function is not smooth and regular distributed.

In conclusion, the results establish that Meshfree can accurately predict displacement, thus it is valuable to further research, the use of Meshfree method in data synthesis, soft tissue simulation and elasticity reconstruction.

While mesh production in complex problems can be a time-consuming and costly effort than the discrete arrangement of equations solution, the Meshfree method presents an attractive substitute to the FE method for solving every type of problems. Meshfree method also appears to carry out the large deformations more naturally as the warp of the cloud of points performs to have a reduced effect on accuracy than in FE. In spite of these advantages, Meshfree methods are more unwieldy to execute and computationally expensive.

References

[1] Bamber J, Cosgrove D, Dietrich CF, Fromageau J, Bojunga J, Calliada F, Cantisani V, Correas JM, D'onofrio M, Drakonaki EE, Fink M. EFSUMB guidelines and recommendations on the clinical use of ultrasound elastography. Part 1: Basic principles and technology. Ultraschall in der Medizin-European Journal of Ultrasound. 2013 Apr;34(02):169-84.

[2] Glaser KJ, Manduca A, Ehman RL. Review of MR elastography applications and recent developments. Journal of Magnetic Resonance Imaging. 2012 Oct 1;36(4):757-74.

[3] Manduca A, Oliphant TE, Dresner MA, Mahowald JL, Kruse SA, Amromin E, Felmlee JP, Greenleaf JF, Ehman RL. Magnetic resonance elastography: non-invasive mapping of tissue elasticity. Medical image analysis. 2001 Dec 31;5(4):237-54.

[4] Asbach P, Klatt D, Hamhaber U, Braun J, Somasundaram R, Hamm B, Sack I. Assessment of liver viscoelasticity using multifrequency MR elastography. Magnetic Resonance in Medicine. 2008 Aug 1;60(2):373-9.

[5] Sporea I, Gilja OH, Bota S, Sirli R, Popescu A. Liver elastography-an update. Medical ultrasonography. 2013 Dec 1;15(4):304.

[6] Naeeni HA, Haghpanahi M. FE Modeling of Living Human Brain Using Multifrequency Magnetic Resonance Elastography. InApplied

Mechanics and Materials 2011 (Vol. 66, pp. 384-389). Trans Tech Publications.

[7] Chen Q, Ringleb SI, Manduca A, Ehman RL, An KN. A finite element model for analyzing shear wave propagation observed in magnetic resonance elastography. Journal of Biomechanics. 2005 Nov 30;38(11):2198-203.

[8] Liu GR, Gu YT. An introduction to meshfree methods and their programming. Springer Science & Business Media; 2005 Dec 5.

[9] Zhu T, Atluri SN. A modified collocation method and a penalty formulation for enforcing the essential boundary conditions in the element free Galerkin method. Computational Mechanics. 1998 Apr 1;21(3):211-22.

[10] Hall TJ, Bilgen M, Insana MF, Krouskop TA. Phantom materials for elastography. ieee transactions on ultrasonics, ferroelectrics, and frequency control. 1997 Nov;44(6):1355-65.

[11] Sinkus R, Tanter M, Xydeas T, Catheline S, Bercoff J, Fink M. Viscoelastic shear properties of in vivo breast lesions measured by MR elastography. Magnetic resonance imaging. 2005 Feb 28;23(2):159-65.